

IMPLEMENTATION AND VALIDATION OF THE SPALART-ALLMARAS TURBULENCE MODEL FOR HIGH SPEED FLOWS

R. Marsilio, D. Grillo

DIASP-Politecnico di Torino, Corso Duca degli Abruzzi 24, 10129 TORINO - ITALY

Keywords: *Turbulence Modeling, Air Breathing Propulsion*

Abstract

The aim of this paper is to develop an axisymmetric numerical procedure, easily extendible to 3-D configurations, based on the Reynolds averaged Navier-Stokes equations coupled with a turbulence model to compute the external flow of a plug nozzle. The governing equations are discretized in the physical domain according to a finite-volume technique with second order accuracy. The turbulence equation written in integral form is solved together with the flow equations. Complex shock-slip surfaces, shock-boundary-layer interactions appear in the flowfield and all the flow discontinuities will be numerically captured.

1 Introduction

Since the direct numerical simulation of turbulence is not possible for practical flow problems due to computer limitations, and as large-eddy simulation has not yet become a practical tool in aerodynamics, the only way to simulate high speed and high Reynolds-number flows is to solve the Reynolds-averaged Navier-Stokes (RANS) equations together with a turbulence model. Turbulence modeling has become one of the key problems in CFD. In aerodynamics, simple algebraic turbulence models have been widely used with fair success. However, the algebraic models are not suitable for handling complex flow situations including flow separation, multiple surfaces with turbulent regions near each

other, or wakes etc. Therefore, the development of turbulence models has been most intensive in the area of transport equation models. The model development has gone towards physically more realistic models on the one hand, to increasing complexity on the other hand.

In practical aerodynamics, a gap has appeared between simple algebraic models with many restrictions and complex transport equation models with difficulty of use and many anomalies. The idea behind the Spalart-Allmaras model [11] is to fill this gap by creating a "local" type transport equation model, which is more sophisticated than algebraic models, but more robust and easier to use than traditional two-equation, or higher degree model. Here the term "local" means that the equation at one point does not depend on the solution at the other points. A typical example of non locality is found in the algebraic Baldwin-Lomax model, where the maximum value of a certain function is found by traversing through the boundary layer and this maximum value is then used as a model parameter. The search for the maximum is typically performed along grid lines perpendicular to the boundary layer. Therefore, these kinds of models are only suited to structured and sufficiently orthogonal grids, and to rather simple boundary-layer-type flows. A local-type model does not suffer from such a restriction and is thus much better suited to handling complex flow problems, where multiple surfaces, multiple boundary layers, separated flow regions, free shear layers or wakes occur.

This paper discusses the implementation of the Spalart-Allmaras turbulence model to a numerical methodology developed to solve complex two-dimensional or axisymmetric flows configurations, [6]. The numerical approach presented is based on a time-dependent integration of the full Navier-Stokes equations where the physical domain is discretized according to a finite volume technique. The convective part of the equations (inviscid fluxes) is treated following a flux difference splitting method with an approximate solution of a Riemann problem at each cell interface [8], [5]. The diffusive terms (viscous fluxes) are calculated using a centered scheme. Second order accuracy is achieved following the guidelines of the essentially non-oscillatory schemes (ENO) [2], with linear reconstruction of the solution inside each cell and at each step of integration. Complex shock-shock and shock-slip surface interactions appear in the flow fields. In our methodology all the shocks and the slip surfaces are numerically captured.

To validate the functionality of the Spalart-Allmaras model the numerical method has been used to solve the turbulent flat plate boundary layer and to solve the turbulent flow over a backward-facing step [7].

All the numerical results carried-out have been compared with theoretical, experimental and direct numerical simulations (DNS) data. The performances of the model in complex flow situations involving shear layer, shock-boundary layer interactions and recirculating flows will be tested by studying the geometry proposed by ONERA [10] for turbulent flows validation where the experimental data are available for comparison.

2 Numerical Method

2.1 Governing Equations

Compressible viscous flows are governed by the Navier-Stokes equations and in particular by the Reynolds-Averaged Navier-Stokes (RANS) equations coupled with the one-equation turbulence equation. All this set of equations may be written in a compact integral conservative form

as:

$$\frac{\partial}{\partial t} \int_V \vec{W} dv + \int_s \vec{F}_I \cdot \vec{n} ds + \int_s \vec{F}_V \cdot \vec{n} ds = \int_V \vec{H} dv \quad (1)$$

where v represents an arbitrary volume enclosed in a surface s . System (1) can be reduced to non-dimensional form with the help of the following reference values: L for length, ρ_∞ for density, T_∞ for temperature, $\sqrt{RT_\infty}$ for velocity, RT_∞ for energy per unit mass and μ_∞ for viscosity. Therefore, from now the flowfield variables should be considered as non-dimensional. In particular, \vec{W} is the hyper-vector of conservative variables, tensor \vec{F}_I contains the inviscid fluxes, tensor \vec{F}_V contains the viscous fluxes and tensor \vec{H} contains the non-homogeneous part of the equations due to the turbulent model:

$$\begin{aligned} \vec{W} &= \{\rho, \rho \vec{q}, E, \tilde{\nu}_T\}^T \\ \vec{F}_I &= \left\{ \rho \vec{q}, p \vec{I} + \rho \vec{q} \otimes \vec{q}, (E + p) \vec{q}, \tilde{\nu}_T \vec{q} \right\}^T \\ \vec{F}_V &= \frac{\sqrt{\gamma M_\infty}}{Re_\infty} \left\{ \vec{0}, -\bar{\tau}, -K \nabla T - \bar{\tau} \cdot \vec{q}, -\frac{\nu + \tilde{\nu}_T}{\sigma} \nabla \tilde{\nu}_T \right\}^T \\ \vec{H} &= \left\{ \vec{0}, \vec{0}, \vec{0}, c_{b1} \tilde{S} \tilde{\nu}_T + \frac{c_{b2}}{\sigma} (\nabla \tilde{\nu}_T)^2 - c_{w1} f_w \left(\frac{\tilde{\nu}_T}{d} \right)^2 \right\}^T \end{aligned} \quad (2)$$

Quantities ρ , p and $\vec{q} = \{u, v, w\}^T$ are the local density, pressure and velocity, respectively; E represents the total energy per unit volume:

$$E = \rho \left(e + \frac{q^2}{2} \right) \quad (3)$$

where e is the internal energy per unit mass, M_∞ and Re_∞ are the freestream Mach number and the Reynolds number, γ is the ratio of the specific heats, $\tilde{\nu}_T$ is the modified eddy viscosity and finally \vec{I} is the unit matrix. The viscous stresses $\bar{\tau}$ are contained in tensor, given by:

$$\tau_{ij} = \mu \left[\frac{\partial q_j}{\partial x_i} + \frac{\partial q_i}{\partial x_j} - \frac{2}{3} (\nabla \cdot \vec{q}) \delta_{ij} \right] - \overline{\rho q_i'' q_j''} \quad (4)$$

The Reynolds-stresses $-\overline{\rho q_i'' q_j''}$ are modeled according to the Boussinesq approximation, which allows one to take the Reynolds-stresses

into account simply by modifying the viscosity. Thus, the viscous stresses can be written as:

$$\tau_{ij} = (\mu + \mu_T) \left[\frac{\partial q_j}{\partial x_i} + \frac{\partial q_i}{\partial x_j} - \frac{2}{3} (\nabla \cdot \vec{q}) \delta_{ij} \right] \quad (5)$$

where $\mu_T = \rho \nu_T$ is a turbulent viscosity coefficient obtained from $\tilde{\mu}_T = \rho \tilde{\nu}_T$. The thermal conductivity K is calculated in non-dimensional form as

$$K = \frac{\gamma}{\gamma - 1} \left(\frac{\mu}{Pr} + \frac{\mu_T}{Pr_T} \right) \quad (6)$$

where Pr and Pr_T are the laminar and turbulent Prandtl numbers. The laminar viscosity μ is computed via Sutherland's law

$$\mu = T^{3/2} \left(\frac{1 + T_{ref}}{T + T_{ref}} \right) \quad (7)$$

with

$$T_{ref} = \frac{110.4}{T_\infty} \quad (8)$$

Finally, the perfect gas relationship $p = \rho T$ completes the set of equations.

2.2 Convective and Diffusive Fluxes

The collapse of such a discontinuity generates in time a pattern of waves along which signals propagate. The waves split the domain in the vicinity of the discontinuity in a set of uniform regions where the values of the flowfield variables are to be computed. Inviscid fluxes \vec{F}_I are evaluated defining and solving an appropriate Riemann problem across each lateral surface. The definition of the Riemann problem consists, at first, in fixing a direction a direction X joining the centroids of the two finite volume that are connected by the considered lateral surface (see Fig.1, left). Then, the variation of the flowfield variables along X is to be considered. Due to the discretization, two piecewise constant (first order accuracy Fig.1, right up) or piecewise linear (second order accuracy, Fig.1, right down) distributions of the flow field variables are present between cells A and B , separated by a discontinuity in correspondence with lateral surface.

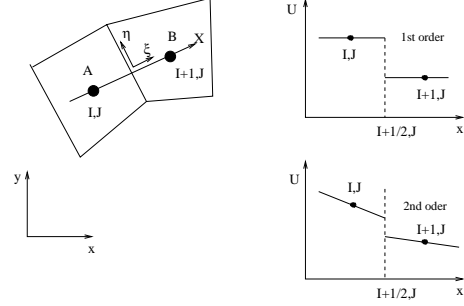


Fig. 1 Riemann problem

The collapse of such a discontinuity generates in time a pattern of waves along which signals propagate. The waves split the domain in the vicinity of the discontinuity in a set of uniform regions where the values of the flowfield variables are to be found, generating in this way a Riemann problem. To obtain waves directions and corresponding signals, the equations governing the inviscid part of the flowfield are written in quasi-linear form in a new local frame of reference constituted by direction ξ and η , which are normal and tangent to the considered lateral surface, respectively. Here an approximated solution of the Riemann problem [8] is sought for, where the shocks which could be generated by the collapse of the initial discontinuities are approximated by compression waves, but the conservative form of the equations ensures that the correct jump and entropy conditions are satisfied. Moreover, the Riemann problem is solved for simplicity in one spatial dimension rather than two, so that only temporal variations of the flowfield variables along the ξ direction are considered. Velocity and temperature gradients needed to evaluate viscous fluxes \vec{F}_V in correspondence with lateral surface are computed through a standard technique that uses central differences and applies the Gauss's Theorem.

Second order accuracy in space and time is achieved following the guideline of the Essentially Non Oscillatory schemes for shock capturing technique [2]. No slip and isothermal or adiabatic conditions are applied to the wall. Freestream conditions are enforced at the inlet, while zero-gradient assumed at the exit boundary for conservative variables.

The eddy viscosity ν_T is obtained from the modified eddy viscosity $\tilde{\nu}_T$, which is solved by the last of the system (1). This equation which is here called the turbulence equation, is basically of similar form to the equations for basic flow variable: mass, momentum and total energy. The only major difference is that the turbulence equation also contains a source term Q inside the vector \vec{H} . The basic source term without transition terms is

$$Q = c_{b1} \tilde{S} \tilde{\nu}_T - \frac{\sqrt{\gamma} M_\infty}{\text{Re}_\infty} c_{w1} f_w \left(\frac{\tilde{\nu}_T}{d} \right)^2 + \frac{\sqrt{\gamma} M_\infty}{\text{Re}_\infty} \frac{c_{b2}}{\sigma} (\nabla \tilde{\nu}_T)^2 \quad (9)$$

where the first term represents production and the second term represents destruction of $\tilde{\nu}_T$. The third term is called the first-order diffusion term. The modified magnitude of vorticity is

$$\tilde{S} = S + \frac{\sqrt{\gamma} M_\infty}{\text{Re}_\infty} \frac{\tilde{\nu}_T}{\kappa^2 d^2} f_{v2} \quad (10)$$

where S is the magnitude of vorticity

$$S = \left| \frac{\partial v}{\partial x} - \frac{\partial u}{\partial y} \right| \quad (11)$$

and d is the distance to the nearest wall. The function:

$$f_{v1} = \frac{\chi^3}{\chi^3 + c_{v1}^3} \quad f_{v2} = 1 - \frac{\chi}{1 + c_{v1} f_{v1}} \quad (12)$$

where $\chi = \tilde{\nu}_T / \nu$. In the destruction term, f_w is defined as:

$$f_w = g \left[\frac{1 + c_{w3}^6}{g^6 + c_{w3}^6} \right]^{1/6} \quad (13)$$

where

$$g = r + c_{w2}(r^6 - r), \quad (14)$$

with

$$r = \frac{\sqrt{\gamma} M_\infty}{\text{Re}_\infty} \frac{\tilde{\nu}_T}{\tilde{S} \kappa^2 d^2} \quad (15)$$

The model coefficients are:

$$\begin{aligned} c_{b1} &= 0.1355, & c_{b2} &= 0.6222, \\ \sigma &= 2/3, & \kappa &= 0.41, \\ c_{w1} &= c_{b1}/\kappa^2 + (1 + c_{b2})/\sigma, & c_{v1} &= 7.1, \\ c_{w2} &= 0.3, & c_{w3} &= 2.0 \end{aligned} \quad (16)$$

The eddy viscosity, or turbulent viscosity, needed in the viscous stress tensor (5) is obtained from

$$\mu_T = \rho f_{v1} \tilde{\nu}_T \quad (17)$$

As boundary conditions free-stream eddy viscosity is specified by setting a value for χ at the free-stream boundaries. Usually it can be set to zero. The eddy viscosity is equal to zero on the surfaces, so its inviscid flux is also zero on the walls.

3 Model validation

3.1 Boundary layer flow

The first test case, used for validation, corresponds to a $M_\infty = 0.3$ flow over an insulated flat plate. In table 1 the freestream conditions for the flow parameters for this case are reported.

M_∞	0.3	
T_∞	300	K
Re/m	10^6	1/m
R	287	J/(Kg K)
γ	1.4	
Pr	0.72	
Pr_T	0.90	

The viscosity is assumed constant in the flow field and its value has been computed with the Sutherland's law at 300K. In these conditions the unit Reynolds number is about $10^6/m$. The computational domain is a rectangular area where the length is $5m$ whereas the width is $0.2m$ (see Fig.2)

The dimension of the computational domain is such as to assure a negligible influence on the boundary layer computation. The numerical solution has been computed on a 100×50 grid. The mesh is characterized by a wall stretching defined by

$$y_j = h \left(1 + \beta \frac{e^{\alpha(1 - \frac{j\Delta h}{h})} - 1}{e^{\alpha(1 - \frac{j\Delta h}{h})} + 1} \right) \quad (18)$$

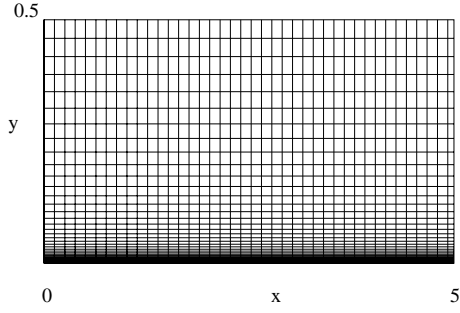


Fig. 2 Flat plate computational grid

where

$$\Delta h = \frac{h}{n_y}, \quad a = -\log\left(\frac{\beta+1}{\beta-1}\right) \quad (19)$$

j being the node index, h the domain width, n_y the total number of cells in y -direction, β a stretching parameter whose value has to be greater than 1. In the present test case the stretching parameter value is set at 1.0001. This value assures that the y^+ value at the first grid point near the wall is approximately 1. Since for this test case the freestream Mach number is very low, the compressibility effects are negligible. For this reason it is possible to compare the numerical results with incompressible boundary layer data. In Fig. 3 the c_f distribution is shown as a function of the Reynolds number Re_x based on the properties at the edge of the boundary layer and the distance from the leading ledge.

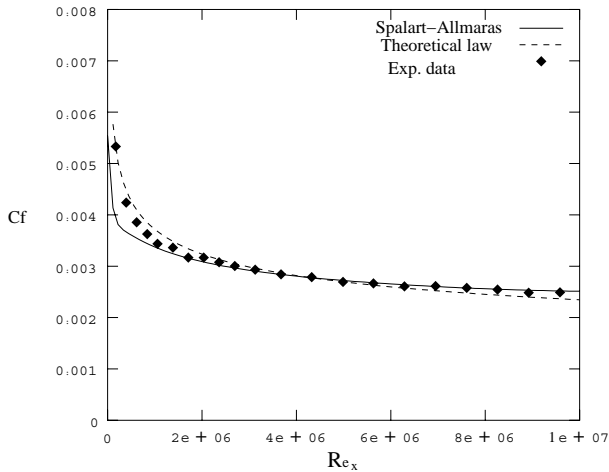


Fig. 3 Turbulent subsonic boundary layer

The results computed by the code are compared with the analytical skin friction coefficient

law for the incompressible turbulent boundary layer flow:

$$c_f = \frac{0.0592}{(R_x)^{0.2}} \quad (20)$$

and the experimental c_f distribution measured by Wieghardt and Tilmann [12]. It is clear that the results are in good agreement with the reference data. In Figs. 4 and 5 the u/U_∞ and u^+ profiles corresponding to the test section at $x = 0.4m$ are shown. As reference data have been considered

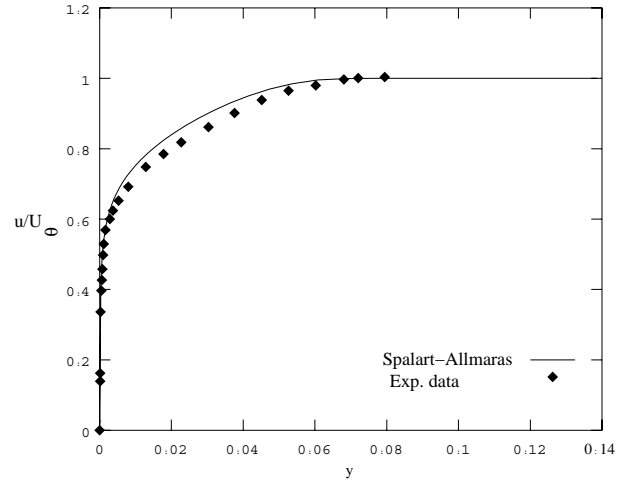


Fig. 4 Velocity profile at $x = 0.4m$

the analytical sublayer law

$$u^+ = y^+ \quad (21)$$

and the log layer law:

$$u^+ = \frac{1}{k} \log(y^+) + 5 \quad (22)$$

and the u^+ profile computed by Wieghardt and Tilmann's experimental data [1]. The data agreement is excellent.

3.2 Turbulent flow over a backward-facing step

Separation and reattachment of turbulent flows occur in many practical engineering application, both in internal flow systems such as diffusers, combustors and channels with sudden expansions and external flows like those around airfoils and buildings. In these situations, the flow experiences an adverse pressure gradient, the pressure

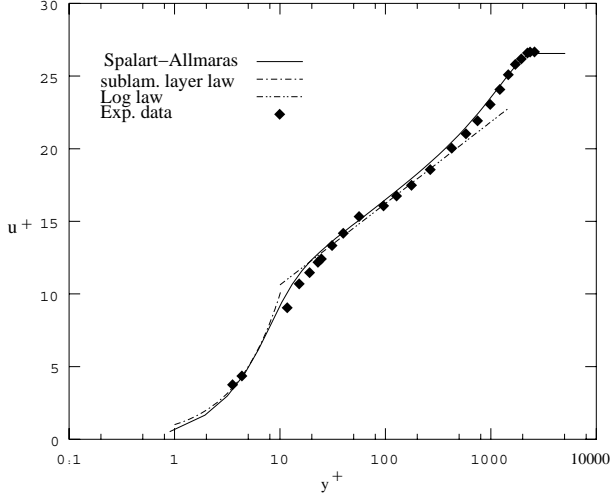


Fig. 5 u^+ profile at $x = 0.4m$

increase in the direction of the flow, which causes the boundary layer to separate from solid surface. The flow subsequently reattaches downstream forming a recirculation bubble. Among the flow geometries used for the studies of separated flows, the most frequently selected is the backward/facing step. Considerable work has been carried out on this flow due to its geometrical simplicity. For such a reason we used this geometry to validate our numerical methodology. Figure 6 shows a schematic view of the flow domain used in this computation.

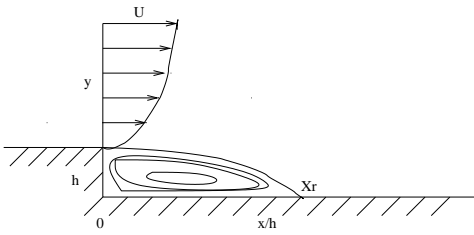


Fig. 6 Backward-facing step configuration

For simplicity, we used a rectangular computational domain starting at the edge of the step ($x = 0$). The coordinate system is placed at the lower step corner as shown in Fig. 6. The mean inflow velocity profile $u(y)$, imposed at the left boundary ($x = 0$) is a computed flat-plate boundary layer profile. To validate the computational results the numerical simulations were carried out for Reynolds number ($Re_h = 5100$) and

compared with the experimental and DNS results [9], [7], [4]. A stretched computational grid in both x and y directions was used. The computed mean reattachment length is $X_r = 6.0h$ comparable with the experimental $X_r = 5.39h$, and the DNS, $X_r = 6.28h$, $X_r = 6.0h$. The reattachment length was demonstrated by Kuen [3] to increase as the expansion ratio increases.

In Fig. 7, the average C_f is compared with DNS and experimental data. Good agreement is

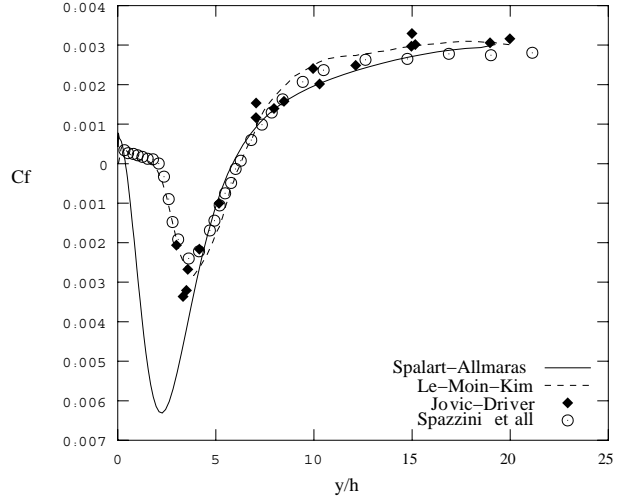


Fig. 7 Comparison between computation DNS and experimental

obtained between computational and experimental data. A striking from previous measurements and the DNS is the large peak of negative skin friction in the recirculation region see in both in our computation and DNS experiment. The Peak negative C_f obtained with our method is about 2 times larger than other results. The secondary vortex in the recirculation bubble is smallest. In fact the Spalart-Allmaras model tends to over estimate the skin friction coefficient when there is a lack of points close to the walls. Figure 8 presents the comparison between computational results, experimental and DNS data. The comparison is made st four representative locations in the recirculation (a), reattachment (b) and recovery regions (c) and (d). Figure 9 compares the computational results with the DNS measurements at $x/h = 19.0$. All profiles are below the universal log-law even at $20h$ downstream of the step. Pre-

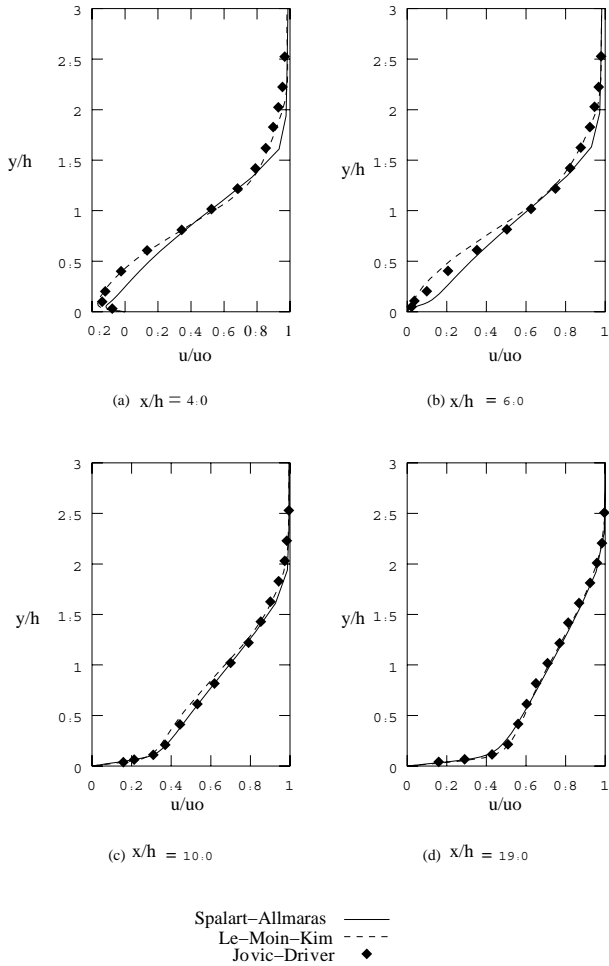


Fig. 8 Mean streamwise velocity profile

vious experimental studies reported a recovery of the log-law profile as early as 6 step heights after the reattachment. The good agreement between the computation and DNS profile at $x/h = 19.0$ confirms that the deviation from the universal log-law is a real effect in this flow. The apparent discrepancy between the present near wall profiles and the experiments is attributed to the method of obtaining the wall-shear velocity u_τ .

4 Plug nozzle results

The numerical simulations of plug nozzle concern a reference plug geometries based on different characteristics of the flow exhausting on the plug wall. The FLOWNET Test-Case P02, proposed by ONERA for CFD validation [10] (P02) has been used. The P02 geometry shown in Fig.10 has been computed with the following

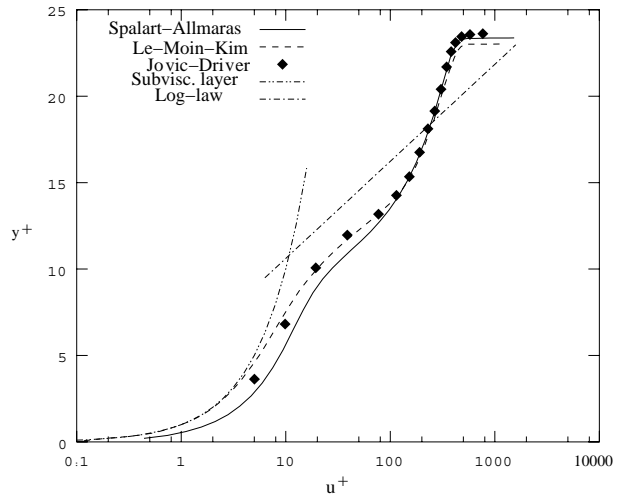


Fig. 9 Mean streamwise velocity profiles in wall coordinates at $x/h = 19.0$

flow conditions, which correspond to the experimental ones: for the external flow we have $M_\infty =$

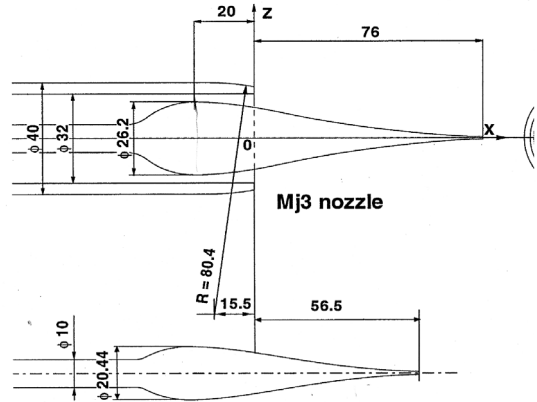


Fig. 10 Flownet Test-Case P02

1.95, stagnation pressure $P^0 = 1 \times 10^5$ Pa and stagnation temperature of 295K; in the jet flow the total pressure is 5×10^5 Pa and the stagnation temperature is 297 K. The Reynolds number is 12.27×10^6 , referenced to the external plug-diameter (40mm). All the computations have been carried out working with cold air ($\gamma = 1.4$). Laminar and turbulent Prandtl number are 0.72 and 0.9 respectively. Adiabatic wall boundary condition has been assumed for the temperature. In Fig.11 the computed Mach number contour-lines are shown. The visualization shows a shock interacting with the external boundary-layer de-

veloping on the boattail. Figure 12 shows the streamlines patterns. After flow separations, occurring near the end of the boattail for the external stream and the nozzle lip for the jet, the flow frontiers envelop a dead water region before co-flowing. The confluence process starts the development of a wake that ensures the mutual adaptation of the flow. In the nozzle exit region, we distinguish the expansion fan centered near the nozzle lip. It is followed by a wave focalization process that creates the classical barrel shock structure of an underexpanded jet. A qualitative analysis with the schlieren photograph taken from Ref.[10] shows a good agreement on the wave behavior. Figure 13 shows a general view of the computed velocity vector field close to the boat-tail region. It is possible to observe the main flow deviation induced by the crossing of either the outer confluence shock or the barrel shock and the progressive mutual adaption of the co-flowing streams along a wake region and the development of the mixing layer.

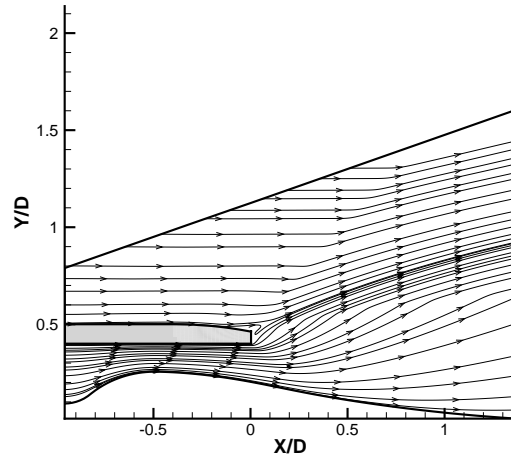


Fig. 12 Streamlines

case agrees very well with the experimental ones and the recirculating bubble close to the boattail is captured correctly. Figure 16 shows also the comparisons in terms of the radial velocity component at the station $x/d = 0.05$.

Figure 17 presents a comparison between the wall computed and the experimental pressure on the boattail, and normalized by the upstream static pressure p_∞ . The aspect of the pressure distribution on the same generating line is typical of an interaction between the external boundary layer and a shock. At first, the approach static pressure is nearly constant and close to 1. The flow expansion induced by the boattail makes the static pressure decrease. Then, at certain location X_0 between -6 and -10 mm, the pressure goes up rapidly when the boundary layer crosses a narrow compression wave system located at the foot of the shock. Figure 18 shows a 3-D sketch of the flow pattern. system located at the foot of the shock.

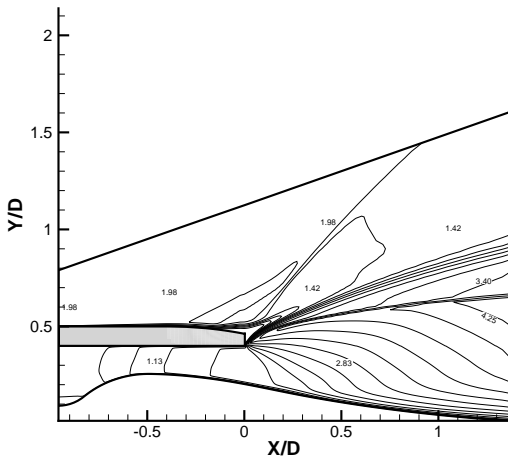


Fig. 11 Mach Number

The comparisons between experimental and numerical data are shown in Figs. 14, 15, 16 and 17. Figures 14 and 15 refer to the comparison of the computed turbulent streamwise velocity (straight lines) and the experimental mean velocity (squares) [10] at stations $x/d = 0.05$ and $x/d = 0.1$. The numerical data for the turbulent

5 Conclusion

A numerical method based on the integration of the unsteady Reynolds Averaged Navier-Stokes Equation has shown to be a suitable tool for plug nozzle analysis and for investigation of the supersonic flow past an axisymmetric afterbody.

The numerical solution of a full length plug

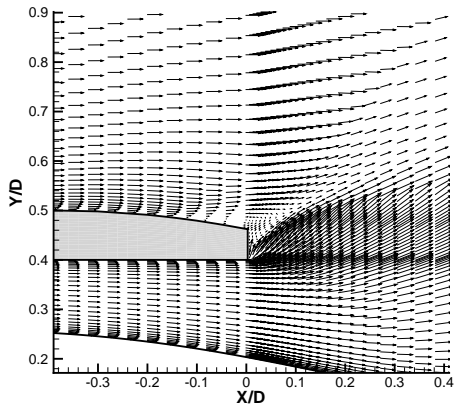


Fig. 13 Computed vector field

nozzle flow field has been investigated and successfully compared to experimental data. The one-equation model of Spalart and Allmaras has shown to capture correctly the flow phenomenology even in the complex flow configurations here presented.

References

- [1] Coles, DA and Hirst EA. Computation of turbulent boundary layer. *Proc 1968 AFOSR-IFP-STANFORD Conference*, Vol. 2, California, USA, 1969.
- [2] Harten, A, Enquist, B, Osher, S, and Chakravarthy SR. Uniformly high accurate essentially non-oscillatory schemes iii. *Journal of Computational Physics*, Vol. 71, 1987.
- [3] Kuehn, DM. Some effects of adverse pressure gradient on the incompressible reattaching flow over a rearward-facing step. *AIAA Journal*, Vol. 18, 1980.
- [4] Jovic, S and Driver, D. Backward-facing step measurement at low reynolds number, $re_h = 5000$. *NACA TM 108807*, 1994.
- [5] Marsilio, R. Vortical solutions in supersonic corner flows. *AIAA Journal*, Vol. 31, pp 1651–1658, 1993.
- [6] Marsilio, R. Numerical simulations for plug nozzle flowfields. *Proc 39th AIAA*, Vol. AIAA Paper 2001-0670, Reno, NV, 2001.
- [7] Moin, P and Kim, J. Direct numerical simu-

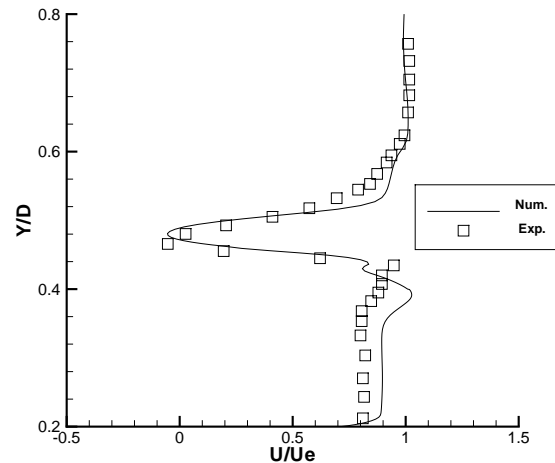


Fig. 14 Axial velocity at $x/d = 0.05$

lation of turbulent flow over a backward-facing step. *Journal of Fluid Mechanics*, Vol. 330, pp 349–374, 1997.

- [8] Pandolfi, M. A contribution to the numerical prediction of unsteady flows. *AIAA Journal*, Vol. 22, pp 37–46, 1983.
- [9] Spazzini, PG, Iuso, G, Onorato, M, Zurlo, N, and Di Cicca GM. Unsteady behaviour of back facing step flow. *Experiments in Fluids*, Vol. 30, pp 551–561, 2001.
- [10] Reijasse, P and Corbel, B. Experimental analysis of the supersonic flow confluence past a jet-on axisymmetric afterbody. *Proc 35th AIAA*, Vol. AIAA Paper 96-2449, Reno, NV, 1996.
- [11] Spalart, P and Allmaras, SR. A one-equation turbulence model fo aerodynamic flows. *La Recherche Aerospaciale*, Vol. 1, pp 5–21, 1994.
- [12] Wieghardt, K and Tilmann, W. On the turbulent layer for rising pressure. *NACA TM 1314*, 1951.

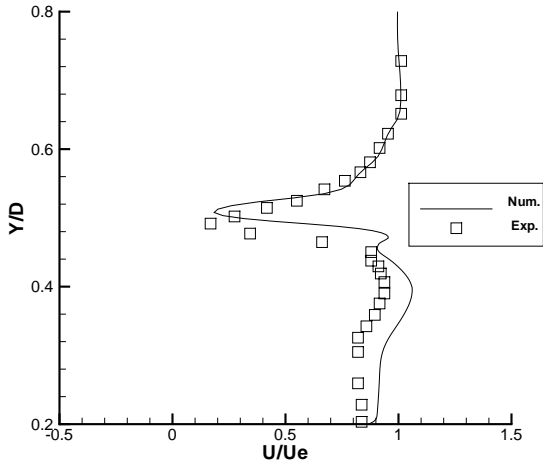


Fig. 15 Axial velocity at $x/d = 0.1$

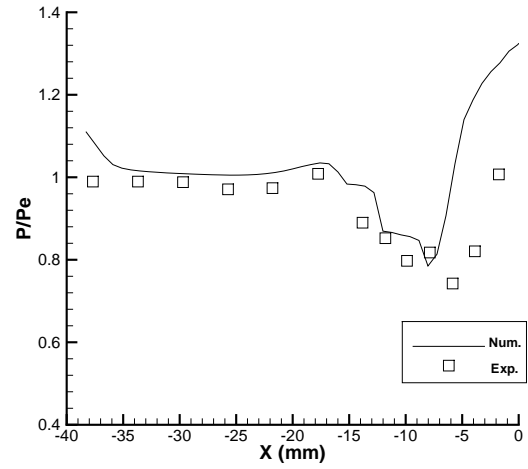


Fig. 17 Wall pressure distribution

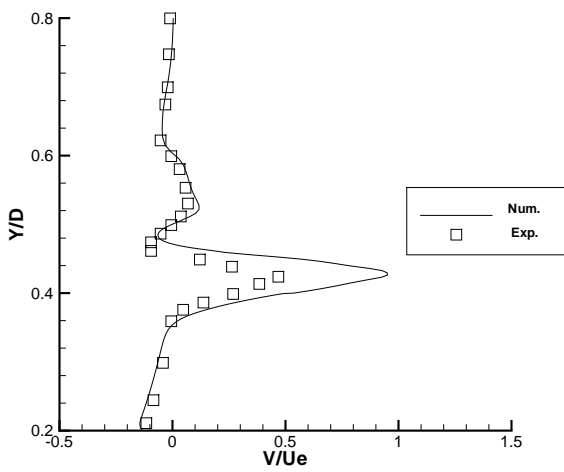


Fig. 16 Radial velocity at $x/d = 0.05$

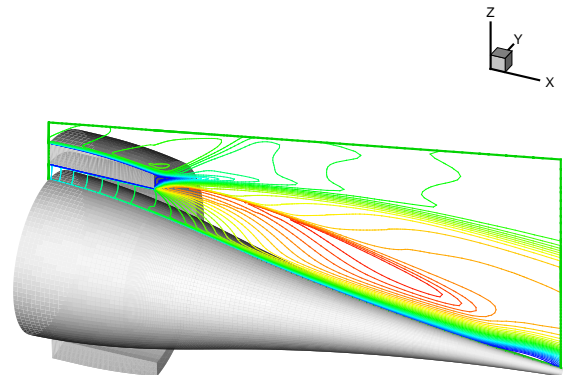


Fig. 18 3-D flow configuration